

1 **Long term variations of actual evapotranspiration over the Tibetan**  
2 **Plateau**

3 Cunbo Han<sup>1,2,3</sup>, Yaoming Ma<sup>1,4,5,6</sup>, Binbin Wang<sup>1,2</sup>, Lei Zhong<sup>7</sup>, Weiqiang  
4 Ma<sup>1,2,4</sup>, Xuelong Chen<sup>1,2,4</sup>, Zhongbo Su<sup>8</sup>

- 5 1. Key Laboratory of Tibetan Environment Changes and Land Surface  
6 Processes, Institute of Tibetan Plateau Research, Chinese Academy of  
7 Sciences, Beijing, China
- 8 2. Land-Atmosphere Interaction and its Climatic Effects Group, State Key  
9 Laboratory of Tibetan Plateau Earth System Science, Institute of Tibetan  
10 Plateau Research, Chinese Academy of Sciences, Beijing, China
- 11 3. Institute for Meteorology and Climate Research, Karlsruhe Institute of  
12 Technology, Karlsruhe, Germany
- 13 4. CAS Center for Excellence in Tibetan Plateau Earth Sciences, Chinese  
14 Academy of Sciences, Beijing, China
- 15 5. University of Chinese Academy of Sciences, Beijing, China
- 16 6. Lanzhou University, Lanzhou, China
- 17 7. Laboratory for Atmospheric Observation and Climate Environment  
18 Research, School of Earth and Space Sciences, University of Science  
19 and Technology of China, Hefei, China
- 20 8. Faculty of Geo-Information Science and Earth Observation, University of  
21 Twente, Enschede, The Netherlands

22

23 **Correspondence to:**

24 Prof. Dr. Yaoming Ma

25 Institute of Tibetan Plateau Research, Chinese Academy of Sciences

26 16-3 Lincui Road, Chaoyang District, Beijing, 100101, China

27 Tel: +86 010 84097079

28 Email: [ymma@itpcas.ac.cn](mailto:ymma@itpcas.ac.cn)

29 **Abstract**

30 Terrestrial actual evapotranspiration ( $ET_a$ ) is a key parameter controlling land-  
31 atmosphere interaction processes and water cycle. However, spatial  
32 distribution and temporal changes of  $ET_a$  over the Tibetan Plateau (TP)  
33 remain very uncertain. Here we estimate the multiyear (2001-2018) monthly  
34  $ET_a$  and its spatial distribution on the TP by a combination of meteorological  
35 data and satellite products. Validation against data from six eddy-covariance  
36 monitoring sites yielded root-mean-square errors ranging from 9.3 to 14.5 mm  
37  $mo^{-1}$ , and correlation coefficients exceeding 0.9. The domain mean of annual  
38  $ET_a$  on the TP decreased slightly ( $-1.45\text{ mm yr}^{-1}$ ,  $p < 0.05$ ) from 2001 to 2018.  
39 The annual  $ET_a$  increased significantly at a rate of  $2.62\text{ mm yr}^{-1}$  ( $p < 0.05$ ) in  
40 the eastern sector of the TP ( $lon > 90^\circ\text{ E}$ ), but decreased significantly at a rate  
41 of  $-5.52\text{ mm yr}^{-1}$  ( $p < 0.05$ ) in the western sector of the TP ( $lon < 90^\circ\text{ E}$ ). In  
42 addition, the decreases in annual  $ET_a$  were pronounced in spring and summer  
43 seasons, while almost no trends were detected in the autumn and winter  
44 seasons. The mean annual  $ET_a$  during 2001-2018 and over the whole TP was  
45  $496 \pm 23\text{ mm}$ . Thus, the total evapotranspiration from the terrestrial surface of  
46 the TP was  $1238.3 \pm 57.6\text{ km}^3\text{ yr}^{-1}$ . The estimated  $ET_a$  product presented in  
47 this study is useful for an improved understanding of changes in energy and  
48 water cycle on the TP. The dataset is freely available at the Science Data  
49 Bank (<http://www.dx.doi.org/10.11922/sciencedb.t00000.00010>, (Han et al.,  
50 [2020](https://doi.org/10.11922/sciencedb.t00000.00010))) and at the National Tibetan Plateau Data Center  
51 (<https://data.tpdc.ac.cn/en/data/5a0d2e28-ebc6-4ea4-8ce4-a7f2897c8ee6/>).

52

53 **Key words:** Actual evapotranspiration; SEBS; Tibetan Plateau; Trend.

54

55

56 **Key points:**

- 57       • The SEBS-estimated monthly  $ET_a$  during 2001-2018 has been  
58       validated against 6 flux towers on the TP.
- 59       • Annual  $ET_a$  over the entire TP and in the western TP decrease  
60       significantly, while it increases in the eastern TP.
- 61       • Decrease of annual  $ET_a$  is pronounced in spring and summer, while  
62       almost no trends are detected in autumn and winter.

63

64

## 65 1 Introduction

66 As the birthplace of Asia's major rivers, the Tibetan Plateau (TP), famous as  
67 the "Water Tower of Asia", is essential to the Asian energy and water cycles  
68 ([Immerzeel et al., 2010](#); [Yao et al., 2012](#)). Along with increasing air  
69 temperature, evidence from the changes of precipitation, runoff, and soil  
70 moisture indicates that the hydrological cycle of the TP has been intensified  
71 during the past century ([Yang et al., 2014](#)). Consuming around two-thirds of  
72 global terrestrial precipitation, evapotranspiration (*ET*) is a crucial component  
73 that affects the exchange of water and energy between the land surface and  
74 the atmosphere ([Oki and Kanae, 2006](#); [Fisher et al., 2017](#)). *ET* is also a key  
75 factor modulating regional and global weather and climate. As one essential  
76 connecting component between the energy budget and the water cycle in the  
77 terrestrial ecosystems ([Xu and Singh, 2005](#)), *ET* and its variations have been  
78 drawing more attention worldwide ([Xu and Singh, 2005](#); [Li et al., 2014](#); [Zhang](#)  
79 [et al., 2018b](#); [Yao et al., 2019](#); [Wang et al., 2020b](#)). Total evaporation from  
80 large lakes of the TP has been quantitatively estimated recently ([Wang et al.,](#)  
81 [2020a](#)), however, the terrestrial *ET* on the TP and its spatial and temporal  
82 changes remain very uncertain.

83

84 Many studies have tried to evaluate *ET*'s temporal and spatial variability  
85 across the TP using various methods. The pan evaporation ( $E_{\text{pan}}$ ), that  
86 represents the amount of water evaporated from an open circular pan, is the  
87 most popular observational data source of *ET*. Long time series of  $E_{\text{pan}}$  are  
88 often available with good comparability among various regional  
89 measurements. Thus, it has been widely used in various disciplines, e.g.,  
90 meteorology, hydrology, and ecology. Several studies have revealed the trend  
91 of  $E_{\text{pan}}$  on the TP ([Zhang et al., 2007](#); [Liu et al., 2011](#); [Shi et al., 2017](#); [Zhang](#)  
92 [et al., 2018a](#); [Yao et al., 2019](#)). Although  $E_{\text{pan}}$  and potential *ET* suggest the

93 long-term variability of  $ET$  according to the complementary relationship (CR)  
94 between  $E_{pan}$  and actual  $ET$  ( $ET_a$ ) ([Zhang et al., 2007](#)), these measures  
95 cannot precisely depict the spatial pattern of trends in  $ET_a$ . Recently, several  
96 studies applied revised models, which are based on the CR of  $ET$ , to estimate  
97  $ET_a$  on the TP ([Zhang et al., 2018b](#); [Ma et al., 2019](#); [Wang et al., 2020b](#)).  
98 Employing only routine meteorological observations without requiring any  
99 vegetation and soil information is the most significant advantage of CR  
100 models ([Szilagyi et al., 2017](#)). However, numerous assumptions and  
101 requirements of validations of key parameters limit the application and  
102 performance of CR models over different climate conditions. The application  
103 of eddy-covariance (EC) technologies in the past decade has dramatically  
104 advanced our understanding of the terrestrial energy balance and  $ET_a$  over  
105 various ecosystems across the TP. However, the fetch of the EC observation  
106 is on the order of hundreds of meters, thus impeding the ability to capture the  
107 plateau-scale variations of  $ET_a$ . Therefore, finding an effective way to advance  
108 the estimation of  $ET_a$  on the TP is of great importance.

109

110 Satellite remote sensing (RS) provides temporally frequent and spatially  
111 contiguous measurements of land surface characteristics that affect  $ET$ , for  
112 example, land surface temperature, albedo, vegetation index. Satellite RS  
113 also offers the opportunity to retrieve  $ET$  over a heterogeneous surface  
114 ([Zhang et al., 2010](#)). Multiple RS-based algorithms have been proposed.  
115 Among these algorithms, the surface energy balance system (SEBS)  
116 proposed by [Su \(2002\)](#) has been widely applied to retrieve land surface  
117 turbulent fluxes on the TP ([Chen et al., 2013b](#); [Ma et al., 2014](#); [Han et al.,](#)  
118 [2016](#); [Han et al., 2017](#); [Zou et al., 2018](#); [Zhong et al., 2019](#)). [Chen et al.](#)  
119 [\(2013b\)](#) improved the roughness length parameterization scheme for heat  
120 transfer in SEBS to expand its modeling applicability over bare ground, sparse

121 canopy, dense canopy, and snow surfaces in the TP. An algorithm for effective  
122 aerodynamic roughness length had been introduced into the SEBS model to  
123 parameterize subgrid-scale topographical form drag ([Han et al., 2015](#); [Han et](#)  
124 [al., 2017](#)). This scheme improved the skill of the SEBS model in estimating  
125 the surface energy budget over mountainous regions of the TP. A recent  
126 advance by [Chen et al. \(2019\)](#) optimized five critical parameters in SEBS  
127 using observations collected from 27 sites globally, including 6 sites on the TP,  
128 and suggested that the overestimation of the global  $ET$  was substantially  
129 improved with the use of optimal parameters.

130

131 While the spatial and temporal pattern of the  $ET_a$  in the TP had been  
132 investigated in many studies ([Zhang et al., 2007](#); [Zhang et al., 2018b](#); [Wang](#)  
133 [et al., 2020b](#)), considerable inconsistencies for both trends and magnitudes of  
134  $ET_a$  exist due to uncertainties in forcing and parameters used by various  
135 models. Thus, in this study, with full consideration of the recent developments  
136 in the SEBS model over the TP, we aim to (1) develop an 18-year (2001-2018)  
137  $ET_a$  product of the TP, along with independent validations against EC  
138 observations; (2) quantify the spatiotemporal variability of the  $ET_a$  in the TP,  
139 and (3) uncover the main factors dominating the changes in  $ET_a$ , using the  
140 estimated product.

141

## 142 **2 Methodology and data**

### 143 **2.1 Model description**

144 The SEBS model ([Su, 2002](#)) was used to derive land surface energy flux  
145 components in the present study. The remote-sensed land surface energy  
146 balance equation is given by

147 
$$R_n = H + LE + G_0. \quad (1)$$

148  $R_n$  is net radiation flux ( $W m^{-2}$ ),  $H$  is sensible heat flux ( $W m^{-2}$ ),  $LE$  is latent  
149 heat flux ( $W m^{-2}$ ), and  $G_0$  is ground heat flux ( $W m^{-2}$ ). Note that this equation  
150 neglected energy stored in the canopy, energy consumption related to freeze-  
151 thaw processes of permafrost and glacier, etc. This equation is not applicable  
152 to any condition where a phase change of water occurs, except the liquid to  
153 vapour phase change.

154

155 The land surface net radiation flux was computed as

156 
$$R_n = (1 - \alpha) \times SWD + LWD - \varepsilon \times \sigma \times T_s^4 \quad (2)$$

157 where  $\alpha$  is the land surface albedo derived from the Moderate Resolution  
158 Imaging Spectroradiometer (MODIS) products. Downward shortwave ( $SWD$ )  
159 and longwave ( $LWD$ ) radiation were obtained from the China Meteorological  
160 Forcing Dataset (CMFD). Land surface temperature ( $T_s$ ) and emissivity ( $\varepsilon$ )  
161 values were also obtained from MODIS products.

162

163 In vegetated areas the soil heat flux,  $G_0$ , was calculated from the net radiation  
164 flux and vegetation cover

165 
$$G_0 = R_n \times (r_c \times f_c + r_s \times (1 - f_c)). \quad (3)$$

166  $r_s$  and  $r_c$  are ratios of ground heat flux and net radiation for surfaces with bare  
167 soil and full vegetation, respectively. Fractional vegetation cover ( $f_c$ ) was  
168 derived from the normalized difference vegetation index (NDVI). Over water  
169 surfaces ( $NDVI < 0$  and  $\alpha < 0.47$ ),  $G_0 = 0.5R_n$  was used ([Gao et al., 2011](#);  
170 [Chen et al., 2013a](#)). On glaciers,  $G_0$  is negligible ([Yang et al., 2011](#)) and  $G_0 =$   
171  $0.05R_n$ .

172

173 In the atmospheric surface layer, sensible heat flux and friction velocity were  
174 calculated based on the Monin-Obukhov similarity ([Stull, 1988](#)),

$$175 \quad U = \frac{u_*}{\kappa} \left[ \ln \left( \frac{z-d_0}{z_{0m}^{eff}} \right) - \psi_m \left( \frac{z-d_0}{L} \right) + \psi_m \left( \frac{z_{0m}^{eff}}{L} \right) \right] \quad (4)$$

$$176 \quad \theta_0 - \theta_a = \frac{H}{\kappa u_* \rho C_p} \left[ \ln \left( \frac{z-d_0}{z_{0h}^{eff}} \right) - \psi_h \left( \frac{z-d_0}{L} \right) + \psi_h \left( \frac{z_{0h}^{eff}}{L} \right) \right] \quad (5)$$

$$177 \quad L = \frac{\rho C_p u_*^3 \theta_v}{\kappa g H}. \quad (6)$$

178  $U$  is the horizontal wind velocity at a reference height  $z$  (m) above the ground  
 179 surface,  $\theta_0$  is the potential temperature at the land surface (K),  $\theta_a$  is the  
 180 potential temperature (K) at the reference height  $z$ ,  $d_0$  is the zero-plane  
 181 displacement height (m),  $\rho$  is the air density ( $\text{kg m}^{-3}$ ),  $C_p$  is the specific heat for  
 182 moist air ( $\text{J kg}^{-1} \text{ }^\circ\text{C}^{-1}$ ),  $\kappa = 0.4$  is the von Kármán's constant,  $u_*$  is the friction  
 183 velocity,  $L$  is the Monin-Obukhov length (m),  $\theta_v$  is the potential virtual  
 184 temperature (K) at the reference height  $z$ ,  $\psi_m$  and  $\psi_h$  are the stability  
 185 correction functions for momentum and sensible heat transfer respectively,  
 186 and  $g$  is the gravity acceleration ( $\text{m s}^{-2}$ ). To account for the form drag caused  
 187 by subgrid-scale topographical obstacles, effective roughness lengths for  
 188 momentum ( $z_{0m}^{eff}$ , m) and sensible heat ( $z_{0h}^{eff}$ , m) transfer were introduced into  
 189 the SEBS model by [Han et al. \(2017\)](#). These modifications are parameterized  
 190 as follows ([Grant and Mason, 1990](#); [Han et al., 2015](#)),

$$191 \quad \ln^2(h/2z_{0m}^{eff}) = \frac{\kappa^2}{0.5D\lambda + \kappa^2 / \ln^2(h/2z_{0m})} \quad (7)$$

$$192 \quad \ln(h/2z_{0h}^{eff} + 1) = \ln(h/2z_{0h} + 1) \frac{\ln(h/2z_{0m} + 1)}{\ln(h/z_{0m}^{eff} + 1)} \quad (8)$$

193 where  $h$  is the average height of the subgrid-scale roughness obstacles,  $\lambda$  is  
 194 the average density of the subgrid-scale roughness elements calculated from  
 195 digital elevation models,  $D$  is the form drag coefficient and  $D=0.4$  is used for  
 196 the mountainous areas of the TP as suggested by [Han et al. \(2015\)](#),  $z_{0m}$  and  
 197  $z_{0h}$  are the local-scale roughness lengths for momentum (m) and heat transfer  
 198 (m), respectively. Detailed calculations can be found in [Su \(2002\)](#). A revised  
 199 algorithm for  $z_{0h}$  developed by [Chen et al. \(2013b\)](#) was applied as this  
 200 algorithm outperforms the original scheme of the SEBS model on the TP.

201



202 To constraint the actual evapotranspiration, the evaporative fraction was  
203 applied in the SEBS model, which is determined by taking energy balance  
204 considerations at dry and wet limiting cases. Under the dry-limit condition, the  
205 evaporation becomes zero due to the limited supply of available soil moisture,  
206 while water vapor evaporates at the potential rate under the wet-limit condition  
207 ([Su, 2002](#)). The evaporative fraction ( $\Lambda$ ) is defined as,

$$208 \quad \Lambda = \frac{LE}{R_n - G_0} \quad (9)$$

209 After calculating evaporative fraction based on the assumption of dry and wet  
210 limits, latent heat flux was calculated by inverting Equation (9). Finally, latent  
211 heat flux was converted to  $ET_a$ . Details are available in [Su \(2002\) and \(Chen  
212 et al., 2013a\)](#). Note that the dry-wet limit assumption did not apply to frozen  
213 soil, water, snow, and ice surfaces. The latent heat flux was obtained as the  
214 residual of the surface energy balance equation (1) after calculating net  
215 radiation, sensible heat flux, and ground heat flux when the dry-wet limit  
216 assumption is not applicable.

## 217 **2.2 Data**

218 In-situ observations, satellite-based products, and meteorological forcing data  
219 were used in this study to estimate monthly  $ET_a$  over the TP area. The CMFD,  
220 that was developed based on the released China Meteorological  
221 Administration (CMA) data ([He et al., 2020](#)), was used as model input. The  
222 CMFD covers the whole landmass of China at a spatial resolution of  $0.1^\circ$  and  
223 a temporal resolution of three hours. The CMFD dataset was established  
224 through the fusion of in-situ observations, remote sensing products, and  
225 reanalysis datasets. In particular, the dataset benefits from the merging of the  
226 observations at about 700 CMA's weather stations, and by using the Global  
227 Energy and Water Cycle Experiment – Surface Radiation Budget (GEWEX-  
228 SRB) shortwave radiation dataset ([Pinker and Laszlo, 1992](#)). The GEWEX-

229 SRB data has not been used in any other reanalysis dataset. In addition,  
230 independent datasets observed in western China where weather stations are  
231 scarce were used to evaluate the CMFD. This includes data collected through  
232 the Heihe Watershed Allied Telemetry Experimental Research (HiWATER) ([Li](#)  
233 [et al., 2013](#)) and the Coordinated Enhanced Observing Period (CEOP) Asia-  
234 Australia Monsoon Project (CAMP) ([Ma et al., 2003](#)). CMFD dataset has been  
235 validated against in situ meteorological observations and compared with other  
236 reanalysis datasets on the TP, demonstrating that it is one of the best  
237 meteorological forcing datasets over the TP area ([Zhou et al., 2016](#); [Xie et al.,](#)  
238 [2017](#); [Wang et al., 2020a](#)). Therefore, it is suitable for this study to drive the  
239 SEBS model. Detailed information for the CMFD dataset is listed in Table 1.  
240

241 MODIS monthly land surface products, including land surface temperature  
242 and emissivity, land surface albedo, and vegetation index, provide land  
243 surface conditions for the SEBS model. Detailed information on MODIS land  
244 surface variables are listed in Table 1. The values of land surface variables in  
245 the MODIS monthly products are derived by compositing and averaging the  
246 values from the corresponding month of MODIS daily files. Validations of  
247 MODIS land surface temperature and albedo against in-situ observations on  
248 the TP suggesting a high quality of MODIS land surface products with low  
249 biases and small root-mean-square errors ([Wang et al., 2004](#); [Ma et al., 2011](#);  
250 [Chen et al., 2014](#)).

251  
252 In-situ EC data observed at six flux stations on the TP were used to validate  
253 model results. Locations of the six observation sites are illustrated in Figure 1  
254 and detailed descriptions for these six sites are shown in Table 2. The  
255 instrumental setup at each site consists of: an EC system comprising a sonic  
256 anemometer (CSAT3, Campbell Scientific Inc) and an open-path gas analyzer

257 (LI-7500, Li-COR); a four-component radiation flux system (CNR-1, Kipp &  
258 Zonen), installed at a height of 1.5 m; a soil heat flux plate (Hukseflux,  
259 HFP01), buried in the soil to a depth of 0.1 m; soil moisture and temperature  
260 probes, buried at a depth of 0.05, 0.10, and 0.15 m, respectively ([Han et al.,  
261 2017](#)). The EC data were processed with the EC software package TK3  
262 ([Mauder and Foken, 2015](#)). The main post-processing procedures of the EC  
263 raw data were as follows: spike detection, coordinate rotation, spectral loss  
264 correction, frequency response corrections ([Moore, 1986](#)), and corrections for  
265 density fluctuations ([Webb et al., 1980](#)). The ground heat flux was obtained by  
266 summing the flux value observed by the heat flux plate and the energy  
267 storage in the layer above the heat flux plate ([Han et al., 2016](#)). A more  
268 comprehensive dataset including the EC data used in this work has been  
269 published and is freely available ([Ma et al., 2020](#)).

270

271 3-hourly CMFD data was averaged into daily and then into monthly data to be  
272 consistent with MODIS products in terms of temporal resolution. Daily land  
273 surface albedo has been averaged into monthly variable. MODIS land surface  
274 products and canopy height data were remapped onto CMFD's grid. Monthly  
275 EC data and in situ meteorological observations, which are used for model  
276 validation, were generated from half-hourly variables.

### 277 **2.3 Model evaluation metrics and data analysis methods**

278 The model performance was assessed using the Pearson correlation  
279 coefficient ( $R$ ), the root-mean-square error (RMSE), and the mean bias (MB)  
280 between the estimated and observed monthly  $ET_a$  at the six stations on the  
281 TP.

282

283 The least-square regression technique was used to detect the long-term linear

284 annual trends in  $ET_a$  values. The linear model to simulate  $ET_a$  values ( $Y_t$ )  
285 against time ( $t$ ) is defined as below and the slope of the linear equation ( $b$ ) is  
286 taken as the changing trend,

$$287 \quad Y_t = Y_0 + bt + \varepsilon_t \quad (10)$$

288

289 The Student's  $t$ -test, having an  $n-2$  degree of freedom ( $n$  is the number of  
290 samples), was used to evaluate the statistical significance of the linear  
291 trends, and only tests with a  $p$ -value less than 0.05 were selected as having  
292 passed the significance test.

### 293 **3 Results and discussion**

#### 294 **3.1 Validation against flux tower observations**

295 The SEBS-estimated  $ET_a$  was validated against EC observations at six flux  
296 stations on the TP at a monthly scale (Figure 2). The SEBS model is capable  
297 of capturing both the magnitude and seasonal variation of the monthly  $ET_a$   
298 signal at all the six stations. The correlation coefficients are all larger than 0.9  
299 and have passed the significance test at the  $p = 0.01$  level. RMSE values  
300 range from 9.3 to 14.5 mm mo<sup>-1</sup> with the minimum at the BJ station and the  
301 maximum at the SETORS station. The MB values are all negative except at  
302 the NADORS station, which means the SEBS model slightly underestimated  
303  $ET_a$  values on the TP.

304

305 Specifically, the SEBS model performed particularly well at the short grass  
306 sites (BJ and NAMORS), with correlation coefficients as high as 0.98 and MB  
307 values below 5.0 mm mo<sup>-1</sup>. At the high grass site (SETORS) and the gravel  
308 site (QOMS), the SEBS model is capable of reproducing the EC-observed  
309 monthly  $ET_a$  with RMSE values of 14.5 and 13.2 mm mo<sup>-1</sup>, respectively. In

310 addition, the underestimates of  $ET_a$  by SEBS are mostly in the dry season,  
311 when the canopy is withered. The validation at the site-scale indicates that the  
312 SEBS model used in this work can be applied to a wide range of ecosystems  
313 over the TP.

### 314 **3.2 Spatial distribution**

315 There was a clear spatial pattern to the multiyear average of annual  $ET_a$   
316 between 2001 and 2018 (Figure 3). In general, the SEBS-estimated  $ET_a$   
317 decreases from the southeast to the northwest of the TP, with the maximum  
318 value above 1200 mm in the southeastern Tibet and Hengduan Mountains  
319 and the minimum value less than 100 mm in the northwestern edge of the TP.  
320 In the central TP, where there are several lakes,  $ET_a$  was typically from 500 to  
321 1000 mm.  $ET_a$  was lower than 200 mm over the high, snow- and ice-bound,  
322 mountainous areas. For example, over the northern slopes of the Himalaya,  
323 Nyenchen Tanglha Mountains, and the eastern section of the Tanggula  
324 Mountains. The reason is that these snow- and ice-bound mountainous areas  
325 have a higher ability to reflect downward shortwave radiation and hence have  
326 less available energy to evaporate. On the whole, the domain averaged  
327 multiyear mean annual  $ET_a$  over the TP is  $496\pm 23$  mm. The total amount of  
328 water evapotranspired from the terrestrial surface of the TP are around  
329  $1238.3\pm 57.6$  km<sup>3</sup> yr<sup>-1</sup>, considering the area of the TP to be  $2.5\times 10^6$  km<sup>2</sup>.

330

331 Figure 4 shows the multi-year average spring (March, April, and May), summer  
332 (June, July, and August), autumn (September, October, and November), and  
333 winter (December, January, and February)  $ET_a$  on the TP. Generally, the  
334 distribution pattern of seasonal  $ET_a$  was comparable with that of the annual  
335  $ET_a$ . Both seasonal and annual  $ET_a$  show a decreasing trend from the  
336 southeastern TP to the northwestern TP. Note that the spatial contrast of  $ET_a$

337 almost faded out in winter season owing to a minimum in available energy  
338 and precipitation (Figure 4d). The  $ET_a$  in spring is higher than that in autumn,  
339 except for some high mountainous areas (e.g.: mountain ranges of Himalaya  
340 and Hengduan mountains). The spring  $ET_a$  ranges from 50 mm to 450 mm,  
341 while autumn  $ET_a$  ranges from 50 mm to 250 mm. In summer, the  $ET_a$  is  
342 larger than 250 mm in most of the TP, while the  $ET_a$  is still below 100 mm in  
343 large areas of the northwestern TP. The multiyear seasonal  $ET_a$  averaged  
344 over the whole TP is  $140\pm 10$  mm,  $256\pm 12$  mm,  $84\pm 5$  mm, and  $34\pm 4$  mm, for  
345 spring, summer, autumn, and winter, respectively.

### 346 3.3 Trend analysis

347 The trend of annual  $ET_a$  during 2001-2018 is shown in Figure 5. Overall, an  
348 increasing trend of SEBS-simulated  $ET_a$  is dominant in the eastern TP (lon >  
349  $90^\circ$  E) while a decreasing trend is dominant in the western TP (lon <  $90^\circ$  E).  
350 The trends pass the  $t$ -test ( $p < 0.05$ ) in most part of the areas. The decreasing  
351 trend in the western TP is pronounced and passes the  $t$ -test ( $p < 0.05$ ). This  
352 trend is larger than  $-7.5$  mm  $yr^{-1}$  in most parts of the area and even larger than  
353  $-10$  mm  $yr^{-1}$  in a few parts. In the eastern TP, the increasing trend is mostly  
354 between 5 and 10 mm  $yr^{-1}$  and passes the  $t$ -test ( $p < 0.05$ ). The  $ET_a$  trend  
355 tends to be greater along the marginal region of the northern, eastern, and  
356 southeastern TP. Along the marginal region of the southwestern TP and in the  
357 western section of Himalaya Mountains this trend weakens.

358

359 The trends of seasonal  $ET_a$  between 2001 and 2018 are spatially  
360 heterogeneous over the TP (Figure 6). Decreasing trends in spring and  
361 summer are generally at a rate between  $-2.5$  and  $-7.5$  mm  $yr^{-1}$ , and increasing  
362 trends are generally at a rate below 5.0 mm  $yr^{-1}$  and 7.5 mm  $yr^{-1}$  in spring and  
363 summer, respectively. Areas showing decreasing  $ET_a$  tend to become larger in

364 autumn and winter seasons. Both the decreasing and increasing trends are  
365 subdued in autumn and winter compared with that in spring and summer  
366 seasons. Decreasing rates of  $ET_a$  in autumn and winter are generally below -  
367 2.5 mm yr<sup>-1</sup>, and only a few areas have a rate larger than -2.5 mm yr<sup>-1</sup>.

368

369 Due to the contrast in the trends in the eastern and western halves of the TP,  
370 we divided the TP into two regions: the eastern TP (lon > 90° E) and the  
371 western TP (lon < 90° E). Trends of the  $ET_a$  anomaly averaged over the entire  
372 TP, the western TP, and the eastern TP are shown in Figure 7a. The domain  
373 means of  $ET_a$  on the TP as a whole, and in the western TP decreased at rates  
374 of -1.45 mm yr<sup>-1</sup> and -5.52 mm yr<sup>-1</sup>, respectively. However, the  $ET_a$  in the  
375 eastern TP increased at a rate of 2.62 mm yr<sup>-1</sup>. The decreasing rate of  $ET_a$  in  
376 the entire TP is influenced mainly by the significant decrease of  $ET_a$  in the  
377 western TP. Seasonally, the rates of change of  $ET_a$  over the whole TP are -  
378 0.82 mm yr<sup>-1</sup> ( $p < 0.05$ ) and -0.79 mm yr<sup>-1</sup> ( $p < 0.05$ ) in spring and summer,  
379 respectively (Figure 7b). However, in autumn and winter the  $ET_a$  changes at a  
380 rate of 0.10 mm yr<sup>-1</sup> and 0.06 mm yr<sup>-1</sup>, respectively, and do not pass the  $t$ -test  
381 ( $p < 0.05$ ).  $ET_a$  in spring and summer seasons account for 75.7% of the  
382 annual  $ET_a$ . The variation in amplitude and changing rates in these two  
383 seasons are much larger than in the other seasons. Moreover, spatial  
384 distributions of spring and summer  $ET_a$  trends are close to that of the annual  
385  $ET_a$  trend (Figure 6). Thus, changes of  $ET_a$  in the spring and summer  
386 dominate the variations of  $ET_a$  in the whole year.

387

388 The decrease of  $ET_a$  over the whole TP and in the western TP during 2001-  
389 2018 can be explained by the decrease of  $R_n$  in the same time period (Figure  
390 8a). From 2001 to 2012,  $ET_a$  averaged over the entire TP increased slightly  
391 and then decreased dramatically from 2012, reaching a minimum in 2014.

392 The significant decrease in  $ET_a$  between 2012 and 2014 was due to the rapid  
393 decline of the  $R_n$  (Figure 8a). In the eastern TP,  $ET_a$  increased during 2001-  
394 2018, while  $R_n$  decreased in the same period. Thus,  $R_n$  was not the dominant  
395 factor controlling the annual variations of  $ET_a$ . However, the increasing trends  
396 of both precipitation and air temperature can explain the increase of  $ET_a$  in the  
397 eastern TP during the period 2001-2018 (Figure 8b and Figure 8c). The  
398 increasing precipitation increased the water resource available for  $ET_a$ .  
399 Moreover, the increasing air temperature accelerated the melting of  
400 permafrost and glaciers on the TP. Hence, the melting water replenished the  
401 ecosystem and increased the  $ET_a$  of the eastern TP.

402

403 Although the domain-averaged trend in  $ET_a$  has been decreasing across the  
404 entire TP from 2001 to 2018,  $ET_a$  values in some areas have increased.  
405 Moreover, the changing rates also depend on the time series of  $ET_a$ . For  
406 example, the  $ET_a$  increased slightly from 2001 to 2012, while decreased from  
407 2001 to 2018. This demonstrates the necessity to evaluate the spatial  
408 distribution of changing trends in  $ET_a$  and utilize long time series to investigate  
409 the trends in  $ET_a$  over the TP.

#### 410 **4 Summary and conclusions**

411 The SEBS-estimated  $ET_a$  is at a resolution of around 10 km, while the  
412 footprint of EC observed  $ET_a$  values ranges from a few dozen meters to a few  
413 hundreds of meters. SEBS-estimated  $ET_a$  compares very well with  
414 observations at the six flux towers, showing low RMSE and MB values. These  
415 estimates were able to capture annual and seasonal variations in  $ET_a$ , despite  
416 these two datasets being mismatched in their spatial representation. Note that  
417 the energy consumption related to freeze-thaw processes and sublimation is  
418 neglected. Thus, the dataset is likely to be less reliable over the glacier,



419 permafrost, and in winter season.

420

421 Heterogeneous land surface characteristics and nonlinear changes in  
422 atmospheric conditions resulted in heterogeneities in spatial distributions of  
423  $ET_a$  and changes in  $ET_a$ . The SEBS-estimated multiyear (2001-2018) mean  
424 annual  $ET_a$  on the TP was  $515 \pm 22$  mm, resulting in approximately  
425  $1287.5 \pm 55.0$  km<sup>3</sup> yr<sup>-1</sup> of total water evapotranspiration from the terrestrial  
426 surface. Annual  $ET_a$  generally decreased from the southeast to the northwest  
427 of the TP. The maximum was over 1200 mm, in the southeastern Tibet and  
428 Hengduan Mountains, while the minimum was less than 100 mm in the  
429 northwest marginal area of the TP. Moreover,  $ET_a$  was typically lower than 200  
430 mm over snow- and ice-bound mountainous areas, as there was limited  
431 available energy to evaporate the water.

432

433 Averaged over the entire TP, annual  $ET_a$  increased slightly from 2001 to 2012,  
434 but decreased significantly after 2012 and reached a minimum in 2014.  
435 Generally, there was a slight decreasing trend in the domain mean annual  $ET_a$   
436 on the TP at the rate of  $-1.45$  mm yr<sup>-1</sup> ( $p < 0.05$ ) from 2001 to 2018. However,  
437 trends of annual  $ET_a$  were opposite in the western and eastern TP. The  
438 annual  $ET_a$  decreased significantly in the western TP at a rate of  $-5.52$  mm yr<sup>-1</sup>  
439 ( $p < 0.05$ ) from 2001 to 2018, while annual  $ET_a$  in the eastern TP increased  
440 at a rate of  $2.62$  mm yr<sup>-1</sup> ( $p < 0.05$ ) in the same period.

441

442 The spatial distributions of seasonal  $ET_a$  trends were also noticeably  
443 heterogeneous during 2001-2018. The spatial patterns of  $ET_a$  trend in spring  
444 and summer were similar to the annual changes in  $ET_a$ .  $ET_a$  decreased as  
445 well in the spring and summer season but at slower rates compared with the  
446 annual  $ET_a$ , however, only very weak trends were found in the autumn and

447 winter seasons.

448

## 449 **5 Data availability**

450 The dataset presented and analyzed in this article has been released and is  
451 available for free download from the Science Data Bank

452 (<http://www.dx.doi.org/10.11922/sciencedb.t00000.00010>, (Han et al., 2020))

453 and from the National Tibetan Plateau Data Center

454 (<https://data.tpdc.ac.cn/en/data/5a0d2e28-ebc6-4ea4-8ce4-a7f2897c8ee6/>).

455 The dataset is published under the Creative Commons Attribution 4.0

456 International (CC BY 4.0) license.

457

## 458 **Acknowledgments**

459 This study was funded by the Second Tibetan Plateau Scientific Expedition  
460 and Research (STEP) program (grant no. 2019QZKK0103), the Strategic  
461 Priority Research Program of Chinese Academy of Sciences (XDA20060101),  
462 the National Natural Science Foundation of China (91837208, 41705005, and  
463 41830650). The CMFD data were obtained from the National Tibetan Plateau  
464 Data Center ([https://data.tpdc.ac.cn/en/data/8028b944-daaa-4511-8769-  
465 965612652c49/](https://data.tpdc.ac.cn/en/data/8028b944-daaa-4511-8769-965612652c49/)). MODIS data were obtained from the NASA Land Processes  
466 Distributed Active Archive Center (<https://lpdaac.usgs.gov/>). Global 1 km  
467 forest canopy height data were obtained from the Oak Ridge National  
468 Laboratory Distributed Active Archive Center for Biogeochemical Dynamics  
469 ([https://daac.ornl.gov/cgi-bin/dsviewer.pl?ds\\_id=1271](https://daac.ornl.gov/cgi-bin/dsviewer.pl?ds_id=1271)). The authors would like  
470 to thank all colleagues working at the observational stations on the TP for their  
471 maintenance of the instruments.

472

473

- 475 Chen, X., Z. Su, Y. Ma, S. Liu, Q. Yu, Z. Xu. 2014. Development of a 10-year (2001-2010) 0.1° data set  
476 of land-surface energy balance for mainland China. *Atmospheric Chemistry and Physics* 14(23):  
477 13097-13117.
- 478 Chen, X., Z. Su, Y. Ma, E. M. Middleton. 2019. Optimization of a remote sensing energy balance method  
479 over different canopy applied at global scale. *Agricultural and Forest Meteorology* 279: 107633-  
480 107633.
- 481 Chen, X., Z. Su, Y. Ma, K. Yang, B. Wang. 2013a. Estimation of surface energy fluxes under complex  
482 terrain of Mt. Qomolangma over the Tibetan Plateau. *Hydrol. Earth Syst. Sci.* 17(4): 1607-1618.
- 483 Chen, X., Z. Su, Y. Ma, K. Yang, J. Wen, Y. Zhang. 2013b. An Improvement of Roughness Height  
484 Parameterization of the Surface Energy Balance System (SEBS) over the Tibetan Plateau. *Journal*  
485 *of Applied Meteorology and Climatology* 52(3): 607-622.
- 486 Fisher, J. B., F. Melton, E. Middleton, C. Hain, M. Anderson, R. Allen, M. F. McCabe, S. Hook, D.  
487 Baldocchi, P. A. Townsend, A. Kilic, K. Tu, D. D. Miralles, J. Perret, J.-P. Lagouarde, D. Waliser, A.  
488 J. Purdy, A. French, D. Schimel, J. S. Famiglietti, G. Stephens, E. F. Wood. 2017. The future of  
489 evapotranspiration: Global requirements for ecosystem functioning, carbon and climate feedbacks,  
490 agricultural management, and water resources. *Water Resources Research* 53(4): 2618-2626.
- 491 Gao, Z. Q., C. S. Liu, W. Gao, N. B. Chang. 2011. A coupled remote sensing and the Surface Energy  
492 Balance with Topography Algorithm (SEBTA) to estimate actual evapotranspiration over  
493 heterogeneous terrain. *Hydrol. Earth Syst. Sci.* 15(1): 119-139.
- 494 Grant, A. L. M., P. J. Mason. 1990. Observations of boundary-layer structure over complex terrain.  
495 *Quarterly Journal of the Royal Meteorological Society* 116(491): 159-186.
- 496 Han, C., Y. Ma, X. Chen, Z. Su. 2016. Estimates of land surface heat fluxes of the Mt. Everest region  
497 over the Tibetan Plateau utilizing ASTER data. *Atmospheric Research* 168: 180-190.
- 498 Han, C., Y. Ma, X. Chen, Z. Su. 2017. Trends of land surface heat fluxes on the Tibetan Plateau from  
499 2001 to 2012. *International Journal of Climatology* 37(14): 4757-4767.
- 500 Han, C., Y. Ma, Z. Su, X. Chen, L. Zhang, M. Li, F. Sun. 2015. Estimates of effective aerodynamic  
501 roughness length over mountainous areas of the Tibetan Plateau. *Quarterly Journal of the Royal*  
502 *Meteorological Society* 141(689): 1457-1465.
- 503 Han, C., Y. Ma, B. Wang, L. Zhong, W. Ma, X. Chen, Z. Su. 2020. The estimated actual  
504 evapotranspiration over the Tibetan Plateau from 2001 to 2018. *VI. Science Data Bank*.  
505 <http://www.dx.doi.org/10.11922/sciencedb.t00000.00010>.
- 506 He, J., K. Yang, W. Tang, H. Lu, J. Qin, Y. Chen, X. Li. 2020. The first high-resolution meteorological  
507 forcing dataset for land process studies over China. *Scientific Data* 7(1): 25-25.
- 508 Immerzeel, W. W., L. P. H. van Beek, M. F. P. Bierkens. 2010. Climate Change Will Affect the Asian  
509 Water Towers. *Science* 328(5984): 1382 LP-1385.
- 510 Li, X., G. Cheng, S. Liu, Q. Xiao, M. Ma, R. Jin, T. Che, Q. Liu, W. Wang, Y. Qi, J. Wen, H. Li, G. Zhu,  
511 J. Guo, Y. Ran, S. Wang, Z. Zhu, J. Zhou, X. Hu, Z. Xu. 2013. Heihe Watershed Allied Telemetry  
512 Experimental Research (HiWATER): Scientific Objectives and Experimental Design. *Bulletin of the*  
513 *American Meteorological Society* 94(8): 1145-1160.
- 514 Li, X., L. Wang, D. Chen, K. Yang, A. Wang. 2014. Seasonal evapotranspiration changes (1983–2006)

515 of four large basins on the Tibetan Plateau. *Journal of Geophysical Research: Atmospheres* 119(23):  
516 13,13-79,95.

517 Liu, X., H. Zheng, M. Zhang, C. Liu. 2011. Identification of dominant climate factor for pan evaporation  
518 trend in the Tibetan Plateau. *Journal of Geographical Sciences* 21(4): 594-608.

519 Ma, N., J. Szilagyi, Y. Zhang, W. Liu. 2019. Complementary-Relationship-Based Modeling of Terrestrial  
520 Evapotranspiration Across China During 1982–2012: Validations and Spatiotemporal Analyses.  
521 *Journal of Geophysical Research: Atmospheres* 124(8): 4326-4351.

522 Ma, W., Y. Ma, H. Ishikawa. 2014. Evaluation of the SEBS for upscaling the evapotranspiration based  
523 on in-situ observations over the Tibetan Plateau. *Atmospheric Research* 138: 91-97.

524 Ma, Y., Z. Hu, Z. Xie, W. Ma, B. Wang, X. Chen, M. Li, L. Zhong, F. Sun, L. Gu, C. Han, L. Zhang, X.  
525 Liu, Z. Ding, G. Sun, S. Wang, Y. Wang, Z. Wang. 2020. A long-term (2005–2016) dataset of hourly  
526 integrated land–atmosphere interaction observations on the Tibetan Plateau. *Earth Syst. Sci. Data*  
527 12(4): 2937-2957.

528 Ma, Y., Z. Su, T. Koike, T. Yao, H. Ishikawa, K. i. Ueno, M. Menenti. 2003. On measuring and remote  
529 sensing surface energy partitioning over the Tibetan Plateau—from GAME/Tibet to CAMP/Tibet.  
530 *Physics and Chemistry of the Earth, Parts A/B/C* 28(1): 63-74.

531 Ma, Y., L. Zhong, B. Wang, W. Ma, X. Chen, M. Li. 2011. Determination of land surface heat fluxes over  
532 heterogeneous landscape of the Tibetan Plateau by using the MODIS and in situ data. *Atmos. Chem.*  
533 *Phys.* 11(20): 10461-10469.

534 Mauder, M., T. Foken. 2015. Eddy-Covariance Software TK3.

535 Moore, C. J. 1986. Frequency response corrections for eddy correlation systems. *Boundary-Layer*  
536 *Meteorology* 37(1): 17-35.

537 Oki, T., S. Kanae. 2006. Global Hydrological Cycles and World Water Resources. *Science* 313(5790):  
538 1068 LP-1072.

539 Pinker, R. T., I. Laszlo. 1992. Modeling Surface Solar Irradiance for Satellite Applications on a Global  
540 Scale. *Journal of Applied Meteorology* 31(2): 194-211.

541 Shi, H., T. Li, G. Wang. 2017. Temporal and spatial variations of potential evaporation and the driving  
542 mechanism over Tibet during 1961–2001. *Hydrological Sciences Journal* 62(9): 1469-1482.

543 Stull, R. B. (1988). An introduction to boundary layer meteorology. Dordrecht, Kluwer Academic  
544 Publishers.

545 Su, Z. 2002. The Surface Energy Balance System (SEBS) for estimation of turbulent heat fluxes. *Hydrol.*  
546 *Earth Syst. Sci.* 6(1): 85-100.

547 Szilagyi, J., R. Crago, R. Qualls. 2017. A calibration-free formulation of the complementary relationship  
548 of evaporation for continental-scale hydrology. *Journal of Geophysical Research: Atmospheres*  
549 122(1): 264-278.

550 Wang, B., Y. Ma, Z. Su, Y. Wang, W. Ma. 2020a. Quantifying the evaporation amounts of 75 high-  
551 elevation large dimictic lakes on the Tibetan Plateau. *Science Advances* 6(26): eaay8558.

552 Wang, G., S. Lin, Z. Hu, Y. Lu, X. Sun, K. Huang. 2020b. Improving Actual Evapotranspiration  
553 Estimation Integrating Energy Consumption for Ice Phase Change Across the Tibetan Plateau.  
554 *Journal of Geophysical Research: Atmospheres* 125(3): e2019JD031799-e032019JD031799.

555 Wang, K., J. Liu, X. Zhou, M. Sparrow, M. Ma, Z. Sun, W. Jiang. 2004. Validation of the MODIS global  
556 land surface albedo product using ground measurements in a semidesert region on the Tibetan

557 Plateau. *Journal of Geophysical Research: Atmospheres* 109(D5).

558 Webb, E. K., G. I. Pearman, R. Leuning. 1980. Correction of flux measurements for density effects due  
559 to heat and water vapour transfer. *Quarterly Journal of the Royal Meteorological Society* 106(447):  
560 85-100.

561 Xie, Z., Z. Hu, L. Gu, G. Sun, Y. Du, X. Yan. 2017. Meteorological Forcing Datasets for Blowing Snow  
562 Modeling on the Tibetan Plateau: Evaluation and Intercomparison. *Journal of Hydrometeorology*  
563 18(10): 2761-2780.

564 Xu, C. Y., V. P. Singh. 2005. Evaluation of three complementary relationship evapotranspiration models  
565 by water balance approach to estimate actual regional evapotranspiration in different climatic  
566 regions. *Journal of Hydrology* 308(1): 105-121.

567 Yang, K., H. Wu, J. Qin, C. Lin, W. Tang, Y. Chen. 2014. Recent climate changes over the Tibetan Plateau  
568 and their impacts on energy and water cycle: A review. *Global and Planetary Change* 112: 79-91.

569 Yang, W., X. Guo, T. Yao, K. Yang, L. Zhao, S. Li, M. Zhu. 2011. Summertime surface energy budget  
570 and ablation modeling in the ablation zone of a maritime Tibetan glacier. *Journal of Geophysical*  
571 *Research: Atmospheres* 116(D14).

572 Yao, T., H. Lu, W. Feng, Q. Yu. 2019. Evaporation abrupt changes in the Qinghai-Tibet Plateau during  
573 the last half-century. *Scientific Reports* 9(1): 20181-20181.

574 Yao, T., L. Thompson, W. Yang, W. Yu, Y. Gao, X. Guo, X. Yang, K. Duan, H. Zhao, B. Xu, J. Pu, A. Lu,  
575 Y. Xiang, D. B. Kattel, D. Joswiak. 2012. Different glacier status with atmospheric circulations in  
576 Tibetan Plateau and surroundings. *Nature Climate Change* 2(9): 663-667.

577 Zhang, C., F. Liu, Y. Shen. 2018a. Attribution analysis of changing pan evaporation in the Qinghai-  
578 Tibetan Plateau, China. *International Journal of Climatology* 38(S1): e1032-e1043.

579 Zhang, K., J. S. Kimball, R. R. Nemani, S. W. Running. 2010. A continuous satellite-derived global  
580 record of land surface evapotranspiration from 1983 to 2006. *Water Resources Research* 46(9).

581 Zhang, T., M. Gebremichael, X. Meng, J. Wen, M. Iqbal, D. Jia, Y. Yu, Z. Li. 2018b. Climate-related  
582 trends of actual evapotranspiration over the Tibetan Plateau (1961–2010). *International Journal of*  
583 *Climatology* 38(S1): e48-e56.

584 Zhang, Y., C. Liu, Y. Tang, Y. Yang. 2007. Trends in pan evaporation and reference and actual  
585 evapotranspiration across the Tibetan Plateau. *Journal of Geophysical Research: Atmospheres*  
586 112(D12).

587 Zhong, L., Y. Ma, Z. Hu, Y. Fu, Y. Hu, X. Wang, M. Cheng, N. Ge. 2019. Estimation of hourly land  
588 surface heat fluxes over the Tibetan Plateau by the combined use of geostationary and polar-orbiting  
589 satellites. *Atmos. Chem. Phys.* 19(8): 5529-5541.

590 Zhou, J., L. Wang, Y. Zhang, Y. Guo, D. He. 2016. Spatiotemporal variations of actual evapotranspiration  
591 over the Lake Selin Co and surrounding small lakes (Tibetan Plateau) during 2003–2012. *Science*  
592 *China Earth Sciences* 59(12): 2441-2453.

593 Zou, M., L. Zhong, Y. Ma, Y. Hu, Z. Huang, K. Xu, L. Feng. 2018. Comparison of Two Satellite-Based  
594 Evapotranspiration Models of the Nagqu River Basin of the Tibetan Plateau. *Journal of Geophysical*  
595 *Research: Atmospheres* 123(8): 3961-3975.

596

597

598 **List of tables**

599 Table 1: Input datasets used in this study. .... 23

600 Table 2: Station information. .... 24

601

602

603

604 Table 1: Input datasets used in this study.

<b>Variables</b>	<b>Data source</b>	<b>Availability</b>	<b>Temporal resolution</b>	<b>Spatial resolution</b>
Downward Shortwave	CMFD	1979 – 2018	3 hours	0.1°
Downward longwave	CMFD	1979 – 2018	3 hours	0.1°
Air temperature	CMFD	1979 – 2018	3 hours	0.1°
Specific humidity	CMFD	1979 – 2018	3 hours	0.1°
Wind velocity	CMFD	1979 – 2018	3 hours	0.1°
Land surface temperature	MOD11C3	2001 – now	Monthly	0.05°
Land surface emissivity	MOD11C3	2001 – now	Monthly	0.05°
Height of canopy	GLAS & SPOT	2000 - now	Monthly	0.01°
Albedo	MOD09CMG	2001 - now	Daily	0.05°
<i>NDVI</i>	MOD13C2	2001 - now	Monthly	0.05°
DEM	ASTER GDEM	-	-	30 m

605

606

607

608 Table 2: Station information.

<b>Station</b>	<b>Location</b>	<b>Elevation (m)</b>	<b>Land cover</b>
QOMS	28.21°N, 86.56°E	4276	Gravel
NAMORS	30.46°N, 90.59°E	4730	Grassy marshland
SETORS	29.77°N, 94.73°E	3326	Grass land
NADORS	33.39°N, 79.70°E	4264	Sparse grass-Gobi
MAWORS	38.41°N, 75.05°E	3668	Sparse grass-Gobi
BJ	31.37°N, 91.90°E	4509	Sparseness meadow

609

610

611



612 **List of figures**

613 Figure 1: Locations of the six flux tower sites (marked by pentagrams) on the  
614 TP. The legend of the color map is elevation above mean sea level in meters.  
615 ..... 26

616 Figure 2: SEBS-estimated and EC-observed monthly  $ET_a$  at the six stations (a-  
617 f) on the TP in years when the latter observations were available. RMSE is the  
618 root-mean-square error, MB is the mean bias, and R is the correlation  
619 coefficient. .... 27

620 Figure 3: Spatial distribution of the SEBS-estimated multiyear (2001-2018)  
621 average annual  $ET_a$ . .... 28

622 Figure 4: Spatial distributions of the SEBS-estimated multiyear (2001-2018)  
623 average seasonal  $ET_a$  (mm/season) values over the TP. (a) spring, (b) summer,  
624 (c) autumn, (d) winter. .... 29

625 Figure 5: Spatial distribution of annual  $ET_a$  linear trend on the TP from 2001 to  
626 2018. The stippling indicates the trends that pass the t-test ( $p < 0.05$ ). .... 30

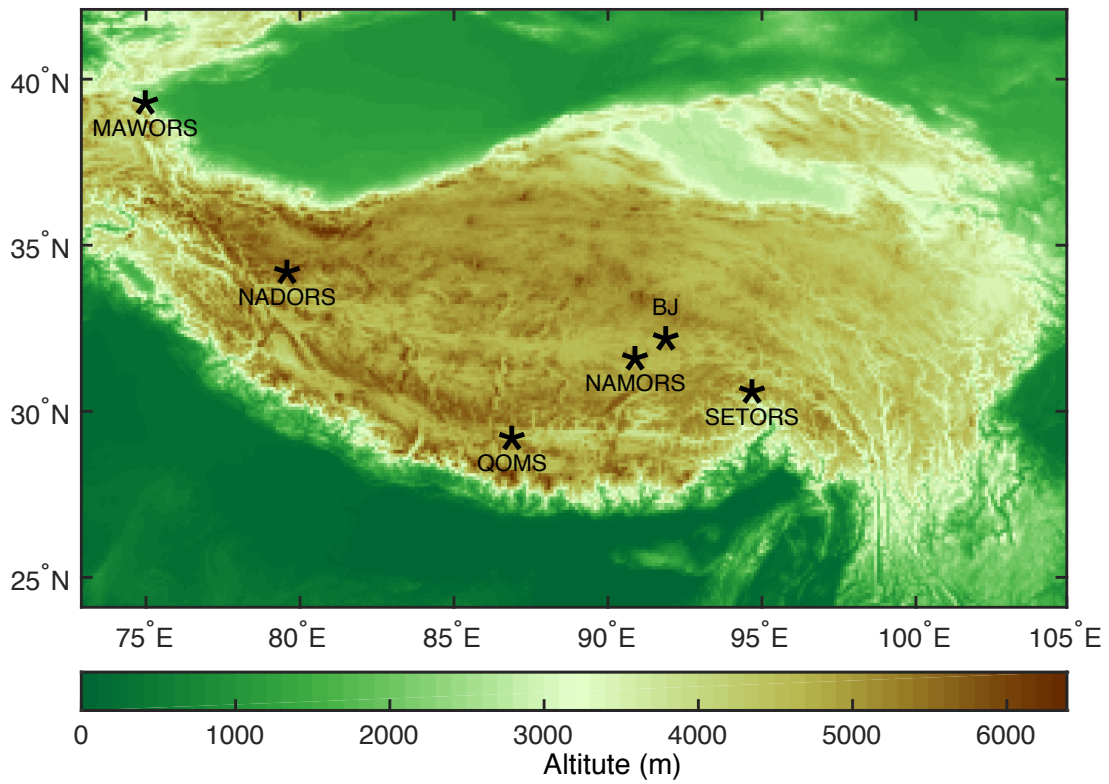
627 Figure 6: Spatial distributions of seasonal  $ET_a$  linear trends on the TP from 2001  
628 to 2018: (a) annual, (b) spring, (c) summer, (d) autumn, (e) winter. The stippling  
629 indicates the trends that pass the t-test ( $p < 0.05$ ). .... 31

630 Figure 7: Anomalies of the domain-averaged annual  $ET_a$  of the entire TP, the  
631 western TP ( $\text{lon} < 90^\circ \text{ E}$ ), and the eastern TP ( $\text{lon} > 90^\circ \text{ E}$ ), respectively (a).  
632 Domain-averaged seasonal  $ET_a$  anomalies over the entire TP (b). The dashed  
633 straight lines indicate linear trends during 2001-2018, and  $k$  is the slope of the  
634 straight line. .... 32

635 Figure 8: Domain-averaged anomalies of annual  $R_n$  (a), precipitation (b), and  
636 temperature (c) over the entire TP, the western TP ( $\text{lon} < 90^\circ \text{ E}$ ), and the eastern  
637 TP ( $\text{lon} > 90^\circ \text{ E}$ ), respectively. The dashed straight lines indicate linear trends  
638 during 2001-2018, and  $k$  is the slope of the straight line. .... 33

639

640

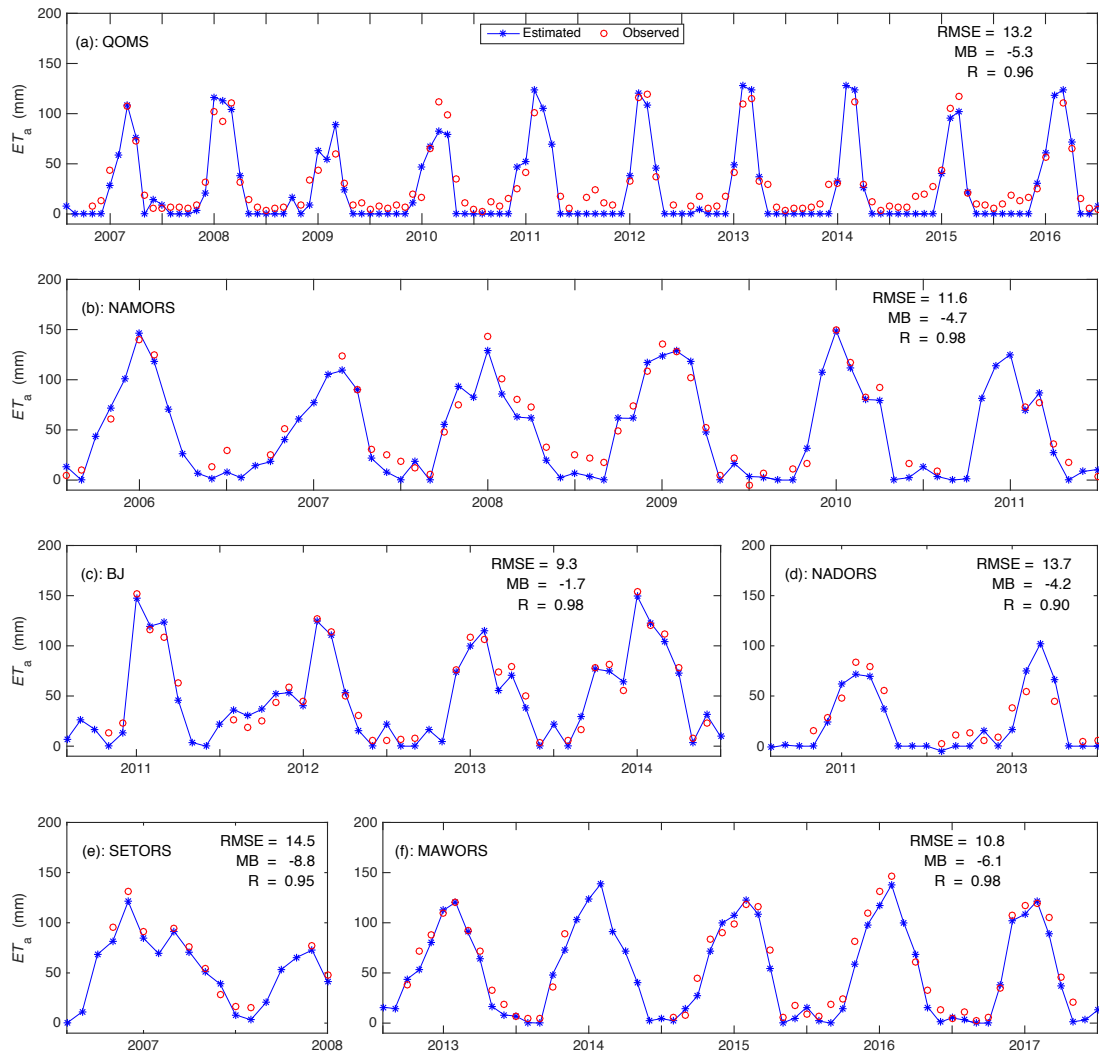


641

642 Figure 1: Locations of the six flux tower sites (marked by pentagrams) on the  
643 TP. The legend of the color map is elevation above mean sea level in meters.

644

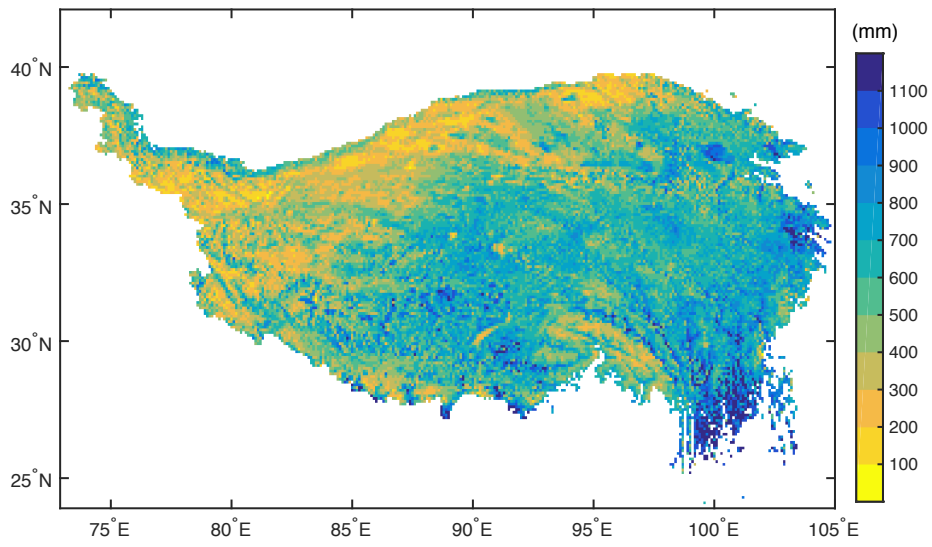
645



646

647 Figure 2: SEBS-estimated and EC-observed monthly  $ET_a$  at the six stations  
648 (a-f) on the TP in years when the latter observations were available. RMSE is  
649 the root-mean-square error, MB is the mean bias, and R is the correlation  
650 coefficient.  
651

652



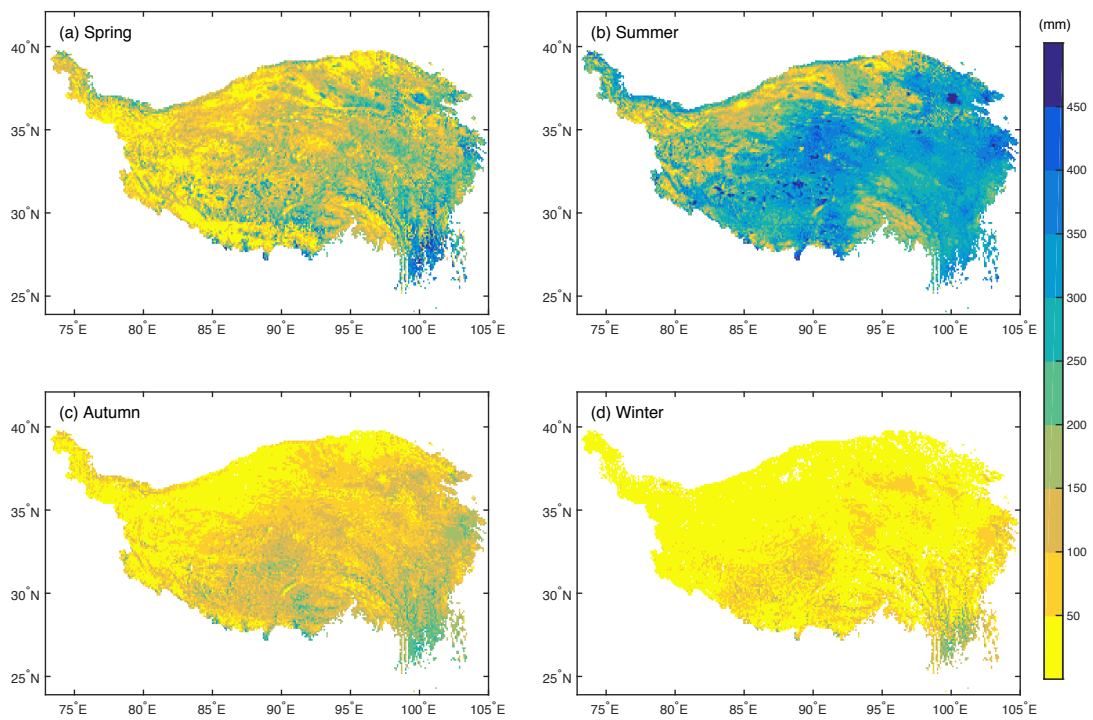
653

654 Figure 3: Spatial distribution of the SEBS-estimated multiyear (2001-2018)

655 average annual  $ET_a$ .

656

657



658

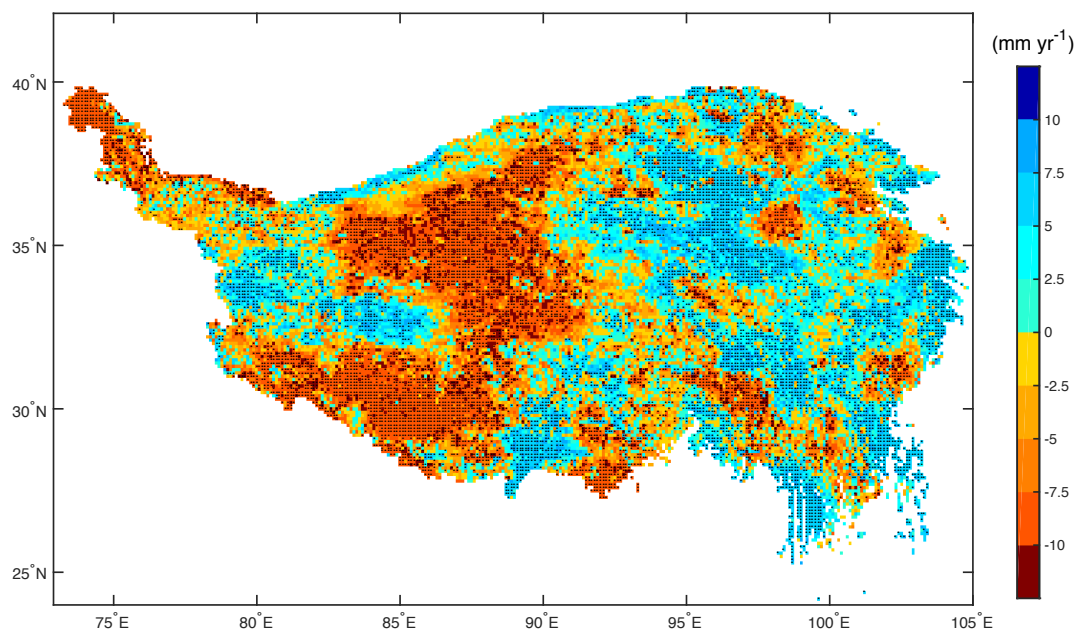
659 Figure 4: Spatial distributions of the SEBS-estimated multiyear (2001-2018)

660 average seasonal  $ET_a$  (mm/season) values over the TP. (a) spring, (b)

661 summer, (c) autumn, (d) winter.

662

663

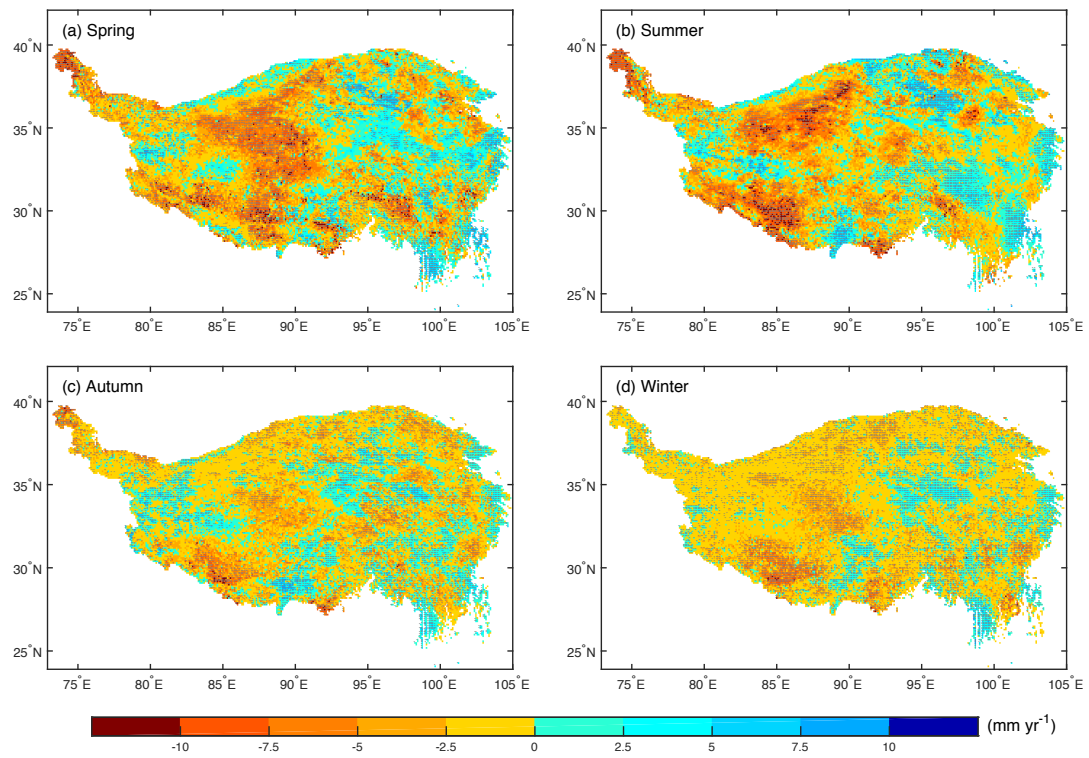


664

665 Figure 5: Spatial distribution of annual  $ET_a$  linear trend on the TP from 2001 to

666 2018. The stippling indicates the trends that pass the t-test ( $p < 0.05$ ).

667

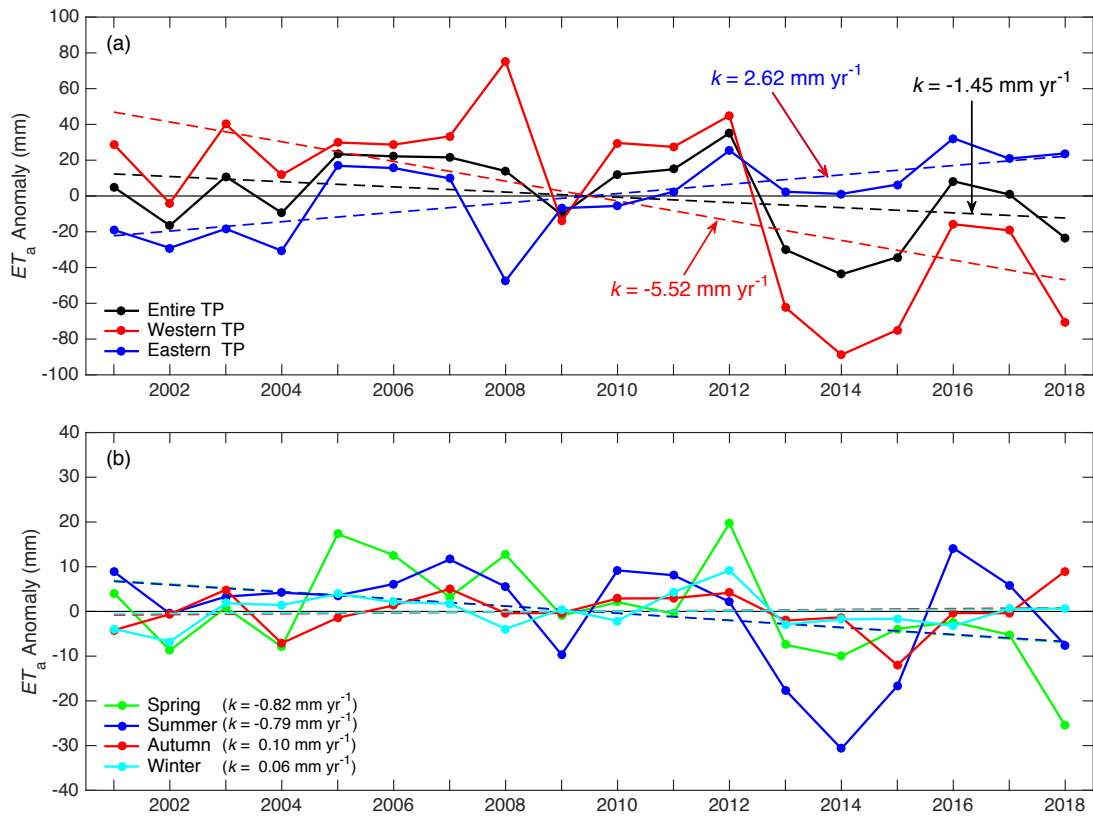


669

670 Figure 6: Spatial distributions of seasonal  $ET_a$  linear trends on the TP from  
 671 2001 to 2018: (a) annual, (b) spring, (c) summer, (d) autumn, (e) winter. The  
 672 stippling indicates the trends that pass the  $t$ -test ( $p < 0.05$ ).

673

674



675

676 Figure 7: Anomalies of the domain-averaged annual  $ET_a$  of the entire TP, the  
677 western TP (lon < 90° E), and the eastern TP (lon > 90° E), respectively (a).

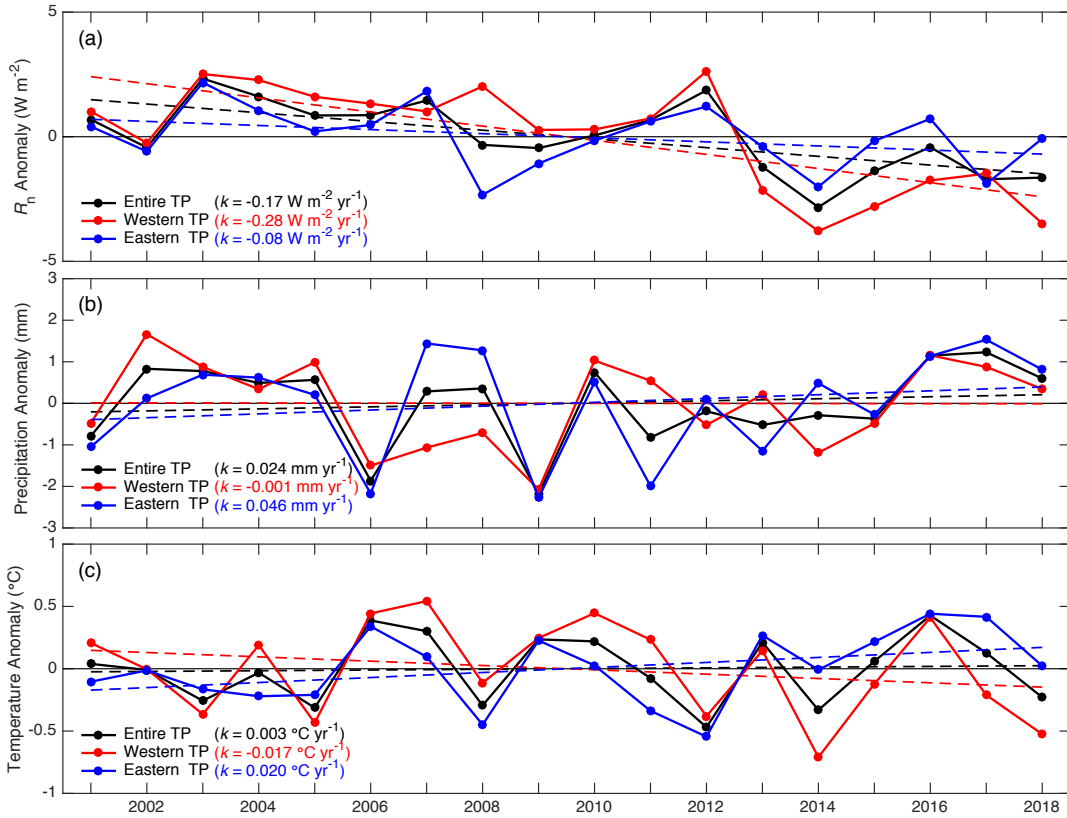
678 Domain-averaged seasonal  $ET_a$  anomalies over the entire TP (b). The dashed  
679 straight lines indicate linear trends during 2001-2018, and  $k$  is the slope of the  
680 straight line.

681

682



683



684

685 Figure 8: Domain-averaged anomalies of annual  $R_n$  (a), precipitation (b), and  
686 temperature (c) over the entire TP, the western TP ( $lon < 90^{\circ} E$ ), and the  
687 eastern TP ( $lon > 90^{\circ} E$ ), respectively. The dashed straight lines indicate  
688 linear trends during 2001-2018, and  $k$  is the slope of the straight line.

689